ARTICLE   OPEN

Check for updates

Prediction of intrinsic topological superconductivity in Mn-doped GeTe monolayer from first-principles

Xiaoming Zhang [1,2,3], Kyung-Hwan Jin [3,4,5], Jiahao Mao[6], Mingwen Zhao[7], Zheng Liu [2✉] and Feng Liu [3✉]

The recent discovery of topological superconductors (TSCs) has sparked enormous interest. The realization of TSC requires a delicate tuning of multiple microscopic parameters, which remains a great challenge. Here, we develop a first-principles approach to quantify realistic conditions of TSC by solving self-consistently Bogoliubov-de Gennes equation based on a Wannier function construction of band structure, in presence of Rashba spin-orbit coupling, Zeeman splitting and electron-phonon coupling. We further demonstrate the power of this method by predicting the Mn-doped GeTe ($Ge_{1-x}Mn_xTe$) monolayer—a well-known dilute magnetic semiconductor showing superconductivity under hole doping—to be a Class D TSC with Chern number of -1 and chiral Majorana edge modes. By constructing a first-principles phase diagram in the parameter space of temperature and Mn concentration, we propose the TSC phase can be induced at a lower-limit transition temperature of ~40 mK and the Mn concentration of x~0.015%. Our approach can be generally applied to TSCs with a phonon-mediated pairing, providing useful guidance for future experiments.

INTRODUCTION

The topological phase of superconductors (SC) has recently received intense research interest as the superconducting quasi-particles residing in the non-trivial gapless/zero-energy boundary states are considered a form of Majorana fermions. Majorana fermions are their own anti-particles[1] and obey the non-Abelian exchange statistics[2], which can be utilized for topological quantum computation[3]. Topological superconductors (TSC) exhibit various exotic phenomena, including zero modes on the magnetic vortex[4], "fractional" Josephson effect[5], non-local correlation[6], and thermal responses[7]. By now, the theoretical aspects of TSCs are reasonably well understood, but the experimental confirmation remains a great challenge due to the requirement of tuning multiple microscopic parameters like the Fermi level, magnetic field, temperature, etc. Hence, it is highly desirable to predict more TSCs and quantify experimental conditions to advance the field.

Unlike the successful first-principles prediction of electronic and topological materials, theoretical predictions of TSCs are challenging because of the uncertainty in the parameters used to construct Bogoliubov-de Gennes (BdG) Hamiltonian. Usually, only the pre-conditions of TSC, e.g., Rashba splitting[8] or topological properties[9–12] in the normal state of known SC, were analyzed using first-principles method, but not the topology of superconducting quasi-particles. Instead, effective models of TSC states are constructed with empirical parameters, at the best partially fit to the first-principles results[13]. Meanwhile, there is a parallel development beyond the mean-field approximation employing more realistic number-conserving approach[14,15], which is yet to be made material specific. Moreover, conventional first-principles approaches that estimate the superconducting transition temperature (T_c) by employing

the empirically McMillan's formula[16] or solving the Migdal-Eliashberg formula[17] cannot be applied to the cases involving spin-orbit coupling (SOC) and magnetism (internal or external). Therefore, more versatile and accurate methods to predict T_c for SC as well as TSC are highly desirable.

In this article, we attempt to further extend first-principles calculations to the field of TSCs, by developing a versatile approach to quantify realistic conditions of TSC. We construct and solve self-consistently a material-specific first-principles BdG Hamiltonian, based on Wannier function (WF) construction of band structure, in presence of Rashba SOC, Zeeman splitting and electron-phonon coupling (EPC). Furthermore, we demonstrate the usefulness of this method by predicting the Mn-doped GeTe ($Ge_{1-x}Mn_xTe$) monolayer to be a TSC by constructing a first-principles phase diagram in the parameter space of temperature and Mn concentration.

Generally, TSC materials can be classified as intrinsic or extrinsic, depending on the experimental conditions of realizing the non-trivial phase. Intrinsic TSCs exhibit inherently a non-trivial superconducting gap without the need of applying an external field or constructing a heterostructure. They may be p-wave SCs with natural spin-triplet pairing[18,19], such as Sr_2RuO_4[20], Cu/Sr/Nb-doped Bi_2Se_3[21] and non-centrosymmetric SCs[22], or s-wave SCs with an effective spin-triplet pairing resulting from helical spin-polarized states, such as the two-dimensional (2D) topological electronic states[23,24], and 1D[25,26] and 2D Rashba electronic states[27–29] which belong to the so-called Class D TSC without time-reversal symmetry (TRS). Extrinsic TSCs employ the same physical mechanisms, but realization of their non-trivial properties requires applying external fields or constructing heterojunctions. To the best of our knowledge, all the known Class D TSCs formed by the s-wave superconductivity are

[1]Department of Physics, College of Information Science and Engineering, Ocean University of China, Qingdao, Shandong, China. [2]Institute for Advanced Study, Tsinghua University, Beijing, China. [3]Department of Materials Science and Engineering, University of Utah, Salt Lake City, Utah, USA. [4]Center for Artificial Low Dimensional Electronic Systems, Institute for Basic Science (IBS), Pohang, Republic of Korea. [5]Department of Physics, Pohang University of Science and Technology, Pohang, Republic of Korea. [6]State Key Laboratory of Low Dimensional Quantum Physics and Department of Physics, Tsinghua University, Beijing, China. [7]School of Physics and State Key Laboratory of Crystal Materials, Shandong University, Jinan, Shandong, China. ✉email: zheng-liu@tsinghua.edu.cn; fliu@eng.utah.edu
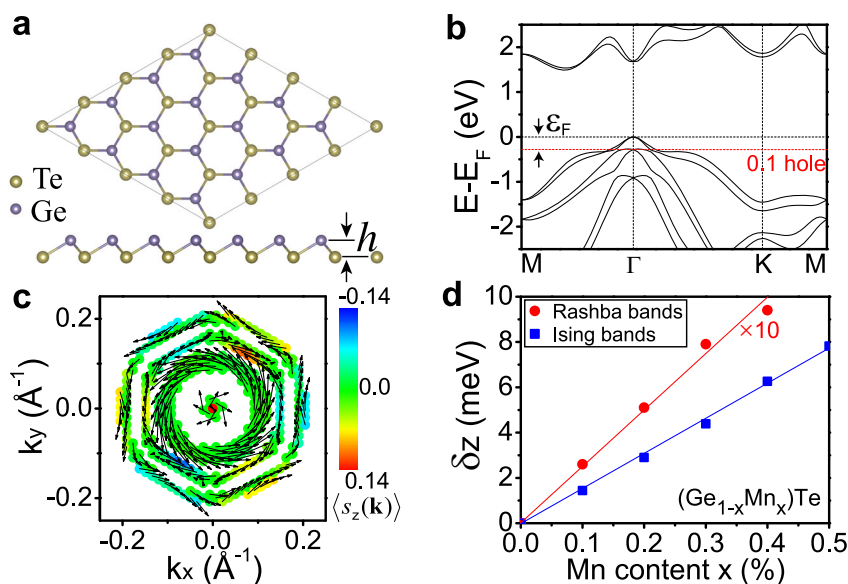
Fig. 1 Crystal structure and electronic property. a The top and side view of GeTe monolayer and (**b**) its electronic band structure. The black horizontal dashed line represents the Fermi level and the red one is the Fermi level after doping 0.1 holes per primitive cell, corresponding to the hole doping concentrations of $\sim7.4\times10^{13}$ cm^{-2}. **c** The electronic spin-texture on the FS of 0.1-hole-doped GeTe monolayer. **d** The Zeeman gaps (δ_z) of the Rashba/Ising bands opened at the Γ point versus the concentration x of Mn dopants with high-spin state. The δ_z of the Rashba bands are magnified by ten times for clarity. The red and blue lines are the linearly fittings of δ_z.

extrinsic, such as the semiconductor nanowire with strong SOC[30], the ferromagnetic atomic chains[31], the nanoscale magnetic islands[32], the ferromagnet[33], and the topological surface[34] and edge states[35] proximitized with conventional SCs with/without applying external magnetic field. Notably, the signature of TSCs observed by applying an external magnetic field in a superconducting material, e.g., FeTe$_{0.55}$Se$_{0.45}$[36], epitaxial GeTe[37] and β-Bi$_2$Pd thin film[38] indicates the possible existence of intrinsic Class D TSC without needing the external magnetic field, which will further enrich the physics of TSC, in the same perspective as from quantum Hall effect (with magnetic field) to anomalous quantum Hall effect (without).

Given the necessary conditions for realizing Class D TSCs with 2D Rashba electrons[27–29], i.e., inversion symmetry breaking, Zeeman gap opening and superconductivity, the IV-VI compound GeTe with Mn doping, a dilute magnetic semiconductors with a ferromagnetic Curie temperatures T_c^{FM} up to ~200 K for epitaxial layers on BaF$_2$ (111) substrate[39–44], caught our attention. The superconductivity of GeTe with p-type doping due to Ge vacancy was confirmed as early as the 1960s[45,46]. It is also known as a ferroelectric material with rhombohedral layered, non-centrosymmetric structure below the ferroelectric Curie temperature of ~700 K[47]. Recently, a gradual opening of Zeeman gap in the Rashba bands of GeTe with Mn doping was observed, attributed to the entanglement of ferromagnetic and ferroelectric order[48]. Also, a recent experiment has reported possible signatures of extrinsic TSC in GeTe film under external magnetic field[37].

Specifically, we focus on the recent experimentally exfoliated GeTe monolayer[49], which was predicted to be useful in optoelectronic devices and may be a type-II Ising superconductor upon slight hole doping[50,51]. We first show that GeTe monolayer inherits all the key characteristics of its bulk phase by using conventional first-principles calculation. Then, the first-principles BdG Hamiltonian was constructed via a WF scheme, through which we found that the GeTe monolayer with the hole concentration of $\sim7.4\times10^{13}$ cm^{-2} becomes superconducting below ~120 mK and the Ge$_{1-x}$Mn$_x$Te monolayer is a Class D TSC with $T_c\sim40$ mK characterized by a non-zero Chern number and

chiral Majorana edge modes. A phase diagram of Ge$_{1-x}$Mn$_x$Te is constructed by employing the developed first-principles approach to guide experimental detection of the predicted SC and TSC phase. Since both the exfoliated GeTe monolayer[49] and epitaxial Ge$_{1-x}$Mn$_x$Te thin film already exist[39–44], our prediction should be readily testable experimentally. Our approach provides a benchmark to make material-specific predictions of TSCs by using first-principles calculations.

RESULTS AND DISCUSSION

Crystal and electronic band structure

The crystal structure of GeTe monolayer is shown in Fig. 1a, which is a (111) layer fragment of its bulk phase. Each Ge(Te) atom is bonded with three Te(Ge) atoms, forming a buckled honeycomb lattice. The in-plane lattice constant a and buckling height h was optimized to be ~3.955 Å and ~1.565 Å, respectively, in good agreement with previous report[50]. Due to the absence of inversion symmetry, a large Rashba splitting arises in the electronic band structure (Fig. 1b). The electronic states are doubly degenerate at the Γ and M points, forming the so-called Kramers pairs, while the degeneracy was lifted away from these time-reversal invariant points. For the four valence bands near the Fermi level of our interest, hereafter we name the lower (upper) two bands as the Rashba (Ising) bands for clarity, referring to their respective electronic spin-texture near the Γ point (Supplementary Fig. 1).

To predict the TSC formed by 2D Rashba electrons[27–29], we focus on the Rashba bands with a significant Rashba splitting coefficient $\alpha_R = 0.66$–0.76 eV Å. It is comparable with that of heavy metals Au(111) and Bi(111) surface[52,53], but slightly smaller than that of bulk GeTe[54]. A strong Rashba effect is desirable for the electrons to overcome the suppressing effect of Zeeman field on superconductivity. Doping 0.1 holes per primitive cell, corresponding to a hole concentration of $\sim7.4\times10^{13}$ cm^{-2}, will move the Fermi level (E_F) to the Dirac point formed by the Rashba splitting (Fig. 1b). The electronic density of states (DOS) at Fermi level, i.e., N_F, is thus increased from 0 to ~1.4 states/eV/primitive-cell, which stems mainly from the p-orbitals of Te and Ge atoms (Supplementary Fig. 2). Figure 1c shows the spin-texture on the Fermi
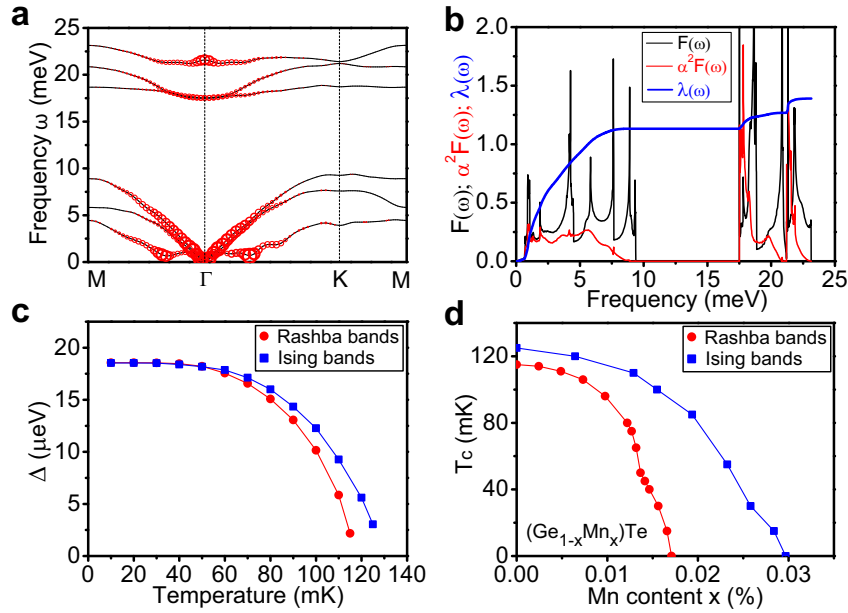
Fig. 2 The superconductivity of 0.1-hole-doped GeTe monolayer without/with Mn dopants. a Phonon spectra with the magnitude of EPC strength $\lambda_{\mathbf{q}v}$ being drawn proportional to the size of red circles. **b** The plots of phonon DOS $F(\omega)$, Eliashberg spectral function $\alpha^2F(\omega)$, and cumulative frequency-dependent EPC strength $\lambda(\omega)$. **c** The temperature-dependent superconducting gap Δ and (**d**) the x-dependent translation temperature T_c of the Rashba bands (red dots) and the Ising bands (blue squares) calculated on $600 \times 600 \times 1$ **k**-points sampling in first BZ.

surfaces (FSs) of the 0.1-hole-doped GeTe monolayer. One can clearly see the in-plane components are helical-like, while the out-of-plane ones are small. The metallic nature and the anti-parallel spins at the **k** and −**k** points provide the prerequisite conditions for s-wave superconductivity.

Having demonstrated the Rashba spin splitting in the GeTe monolayer, we now discuss the second ingredient, the Zeeman gap. It has been reported that a Zeeman gap can be opened in the bulk $Ge_{1-x}Mn_xTe$ with a ferromagnetic order parallel to the (111) direction[48], which is the easy magnetization direction for small x[55]. By reproducing the experimental results of bulk $Ge_{1-x}Mn_xTe$ based on the virtual crystal approximation (VCA)[56], the spin state of Mn dopants was determined to be $S = 5/2$ (Supplementary Note 1). Consequently, the out-of-plane high-spin state ($S = 5/2$) of Mn dopants is adopted in $Ge_{1-x}Mn_xTe$ monolayer under VCA. As expected, the Zeeman gaps δ_z of Rashba and Ising bands opened at Γ increase monotonically with the increasing Mn concentration (Fig. 1d), and can be fit by the equation of $\delta_z = 250 \times x$ and $\delta_z = 1550 \times x$ meV, respectively. The different slopes are the result of different out-of-plane spin magnitude of the electronic states near the Dirac point versus near the valance band maximum (Supplementary Fig. 1c).

Superconductivity with and without TRS

We next discuss the phonon-mediated superconductivity of the 0.1-hole-doped GeTe monolayer. From the calculated phonon spectra (Fig. 2a), we first confirm its dynamical stability by the absence of imaginary frequency. For the acoustic branch with the lowest vibration frequency, Kohn anomalies can be seen at certain **q**-points around Γ, which is favorable for enhancing EPC. Then the EPC strength is evaluated based on the conventional first-principles approach (see Methods sections). The calculated EPC strength $\lambda_{\mathbf{q}v}$ of a specific phonon mode v at the wavevector **q** with the frequency $\omega_{\mathbf{q}v}$ shows two significant features (Fig. 2a). On one hand, all phonon modes can couple with electrons. This is further confirmed by the comparison between the frequency ω dependent phonon DOS $F(\omega)$ and isotropic Eliashberg spectral function

$\alpha^2F(\omega)$, where α^2 is the average of electron-phonon interaction (Fig. 2b). Meanwhile, the cumulative EPC strength $\lambda(\omega)$ increases quickly to 1.13 at the frequency of $\omega \sim 10$ meV, which is about 81% of the total EPC constant $\lambda = 1.39$. This indicates that the EPC stems mainly from the acoustic modes. The convergence of EPC calculation has been carefully checked (Supplementary Note 2). On the other hand, only the vibration modes with a finite wave vector can couple with electrons. This is because for all the FS contours surrounding Γ (Fig. 1c), only a finite length of phonon wave vectors can connect the initial and final scattering states. In addition, both $\alpha^2F(\omega)$ and $\lambda_{\mathbf{q}v}$ illustrate that the soft modes associated with the Kohn anomalies help to enhance the EPC strength[57].

To estimate the superconducting transition temperature T_c, we construct a material-specific BdG Hamiltonian $H_{BdG}(\mathbf{k})$ in the momentum space by employing the electronic Hamiltonian $H_{WFs}(\mathbf{k})$:

$$H_{BdG}(\mathbf{k}) = \begin{pmatrix} H_{WFs}(\mathbf{k}) - E_F & \\ & -H^*_{WFs}(-\mathbf{k}) + E_F \end{pmatrix} + H_\Delta \quad (1)$$

$$H_\Delta = \Delta\left(\varphi^\dagger_{i\uparrow}\varphi^\dagger_{i\downarrow} - \varphi^\dagger_{i\downarrow}\varphi^\dagger_{i\uparrow}\right) + \Delta\left(\varphi_{i\downarrow}\varphi_{i\uparrow} - \varphi_{i\uparrow}\varphi_{i\downarrow}\right) \quad (2)$$

Here the $H_{WFs}(\mathbf{k})$ is obtained by the Fourier transform of the real-space Hamiltonian $H^{(\mathbf{R})}_{WFs}$, and the latter can be constructed from fitting the first-principles band structure of specific materials using WANNIER90 code under the basis of WFs[58]. Each WF with the orbital index i contains two spin-components, leading to $2\aleph$ total WFs. The chemical potential E_F in $H_{BdG}(\mathbf{k})$ is the Fermi level where the superconducting gap Δ condenses under the basis vector of $\varphi_{BdG} = (\varphi_{WFs}, \varphi^\dagger_{WFs})^T$. Only the intra-orbital spin-singlet pairing is considered in the $H_{BdG}(\mathbf{k})$ following the previous theoretical proposals[27–29]. Then we formulate the superconducting gap equation into the following form:

$$\Delta_{ij} = -\frac{g_{ij}}{2V}\sum_{l,\mathbf{k}>0}\frac{1}{1+e^{\beta E_{l,\mathbf{k}}}}\frac{\partial E_{l,\mathbf{k}}}{\partial \Delta_{ij}} \text{ with } \beta = \frac{1}{k_BT} \quad (3)$$

Here $E_{l,\mathbf{k}}$ are eigenvalues of the so constructed $H_{BdG}(\mathbf{k})$. V, l, k_B, and T represent material volume, band index of quasi-particles, Boltzmann constant and temperature, respectively. The intra-orbital spin-singlet pairing in the form of Eq. 2 ensures $i = j$, i.e., $\Delta_{ii} \equiv \Delta$. The absolute pairing strength g_{ii} is usually identical for the bands with similar orbital character in one specific material[57], which is calculated as $g_{ii} = (\lambda - \mu^*)/N_F \equiv g$ with μ^* representing effective Coulomb repulsion[59]. This gap equation enables us to solve the superconducting gap self-consistently at different temperatures. Only the quasi-particle states within one Debye temperature θ_D around zero energy, i.e., $|E_{l,\mathbf{k}}| \leq \theta_D$, are summed over in the $\mathbf{k} > 0$ half of Brillouin zone (BZ) considering the particle-hole symmetry of $H_{BdG}(\mathbf{k})$. Details of constructing the BdG Hamiltonian $H_{BdG}(\mathbf{k})$ and formulating the gap equation can be found in the Methods sections.

We emphasize that this method is not only different from the conventional method employing the McMillan's formula[16] or solving the anisotropic Migdal-Eliashberg formula[17] in estimating T_c, but also extend the first-principles approach to calculate the topological invariant of superconducting gap and the critical magnetic field/doping-concentration of superconductivity (see below). We check the correctness of Eq. 3 by reducing it to the well-known gap equation of $1 = \frac{g}{V} \sum_{\mathbf{k} > 0} \frac{1}{\sqrt{\Delta^2 + \varepsilon_{\mathbf{k}}^2}} \tanh\left(\frac{\beta}{2}\sqrt{\Delta^2 + \varepsilon_{\mathbf{k}}^2}\right)$ for a single-band s-wave SC[60]. Here $\varepsilon_{\mathbf{k}}$ are eigenvalues of normal electronic state; details are given in the Methods sections. Its reliability is further confirmed by reproducing superconductivity of three representative known SCs, i.e., bulk lead (Supplementary Fig. 4)[61], bulk GeTe (Supplementary Fig. 3d)[46], and MoS_2 monolayer (Supplementary Fig. 5)[62,63]. In the calculations, the Debye temperature θ_D of ~105, ~200, and ~300 K is employed for lead, GeTe, and MoS_2 monolayer[64,65], respectively. The weak Coulomb screening effect was considered by using $\mu^* = 0.2$ for bulk GeTe with the hole doping concentration of 2.1×10^{21} cm^{-3}[46] and the electron-electron correlation was considered by reducing EPC constant by ~45.5% for MoS_2 monolayer with electron doping concentration of 1.2×10^{14} cm^{-2}[66]. Details can be seen form Supplementary Note 3.1.

For the 0.1-hole-doped GeTe monolayer, we assume the Debye temperature (~200 K) and Coulomb repulsion μ^* to be same as that of bulk GeTe and extract the WFs using the p orbitals of Ge and Te. Also, we heuristically reduce the calculated total EPC constant λ from 1.39 to ~0.76 by ~45.5%, based on the benchmark of correlation effect in MoS_2 monolayer[66]. This should set a lower limit on EPC constant since the correlation effect of p-orbitals is usually weaker than that of d-orbitals. The resulting absolute pairing strength g (~0.4) is comparable to that of bulk GeTe (~0.49)[67], which enables us to predict the superconducting gap Δ of the 0.1-hole-doped GeTe monolayer at different temperatures. From Fig. 2c, one can see the calculated Δ ~18.6 μeV for both Rashba and Ising bands, which is gradually suppressed with the increasing temperature. The T_c is around ~120 mK, lower than that of GeTe film[46]. We anticipate that the predicted 2D superconductivity may be confirmed by growing GeTe monolayer on Si (111) wafers, as the epitaxial GeTe thin film was observed to be superconducting on this substrate[37].

Next we simulate the superconductivity of $Ge_{1-x}Mn_xTe$ monolayer by adding an out-of-plane Zeeman energy B_z in $H_{WFs}(\mathbf{k})$ first:

$$H_{WFs}^z(\mathbf{k}) = B_z\sigma_z \otimes I_{\aleph \times \aleph} + H_{WFs}(\mathbf{k}) \qquad (4)$$

Here σ_z is the Pauli matrix in spin space and the $I_{\aleph \times \aleph}$ is a $\aleph \times \aleph$ identity matrix. Then the BdG Hamiltonian $H_{BdG}^z(\mathbf{k})$ can be reconstructed through the Eq. 1 and Eq. 2. The reliability of such treatment in simulating the SC without TRS is confirmed by reproducing the in-plane critical magnetic field of MoS_2 monolayer (Supplementary Note 3.2).[68]

By diagonalizing the $H_{WFs}^z(\mathbf{k})$ with different B_z in momentum-space, we obtain the Zeeman gap δ_z' of Rashba and Ising bands opened at Γ point (Supplementary Fig. 6a), which can be fit as $\delta_z' = 0.122 \times B_z$ and $\delta_z' = 2.0 \times B_z$ meV, respectively. Combining with the δ_z fit to the first-principles results in Fig. 1d, one obtains the relationship between B_z and Mn concentration, as $B_z = 2049 \times x$ and $B_z = 775 \times x$ meV for the Rashba and Ising bands, respectively. The self-consistently calculated T_c (Supplementary Fig. 6b) and Δ (Supplementary Fig. 6c) demonstrate that they both decrease gradually with the increasing B_z due to the pairing breaking effect of magnetism. The superconductivity of Rashba (Ising) bands is fully suppressed when $B_z > 0.35$ (0.23) meV, indicating a critical Mn doping concentration of $x_c \sim 0.017\%$ (0.03%) (Fig. 2d). This value of x_c is two orders of magnitude smaller than that (2%) of Mn doped MgB_2[69], which is reasonable since the T_c of GeTe monolayer is lower than MgB_2 by similar magnitude.

Topological superconductivity and phase diagram

To realize TSC formed by 2D Rashba electrons, model analysis proposes that the half of the Zeeman gap opened at the Dirac point of Rashba bands, i.e., $\delta_z/2$, should be larger than the superconducting gap Δ[27–29]. In the following, the first-principles approach has been extended to characterize the TSC phase based on a material-specific BdG Hamiltonian $H_{BdG}^z(\mathbf{k})$. Specifically, we take $\Delta = 0.2$ meV and $B_z = 7.5$ meV with $\delta_z \sim 0.9$ meV to construct the $H_{BdG}^z(\mathbf{k})$ of $Ge_{1-x}Mn_xTe$ monolayer via Eq. 1, Eq. 2 and Eq. 4. The relatively large B_z and Δ are used to show the topological non-triviality more clearly. The $H_{BdG}^z(\mathbf{k})$ is analogous to the single-particle Hamiltonian of electrons with an energy gap mathematically. By diagonalizing $H_{BdG}^z(\mathbf{k})$ in the momentum space, we obtain the dispersion relation of superconducting quasi-particles (Fig. 3a). One can clearly see that the superconducting gap is indeed opened, where the topological invariant, i.e., first Chern number (N_c), is well-defined.

For 2D systems, the Chern number of l-th band is calculated by integrating the Berry curvature $\Omega^l(\mathbf{k}) = \nabla \times A^l(\mathbf{k})$ over the first BZ: $N_c^l = \frac{1}{2\pi} \int_{BZ} \Omega^l(\mathbf{k}) d^2\mathbf{k}$, where $A^l(\mathbf{k})$ is Berry connection. The total Chern number N_c can be obtained by summing up the Chern numbers of all the states below the superconducting gap, which is quantized to −1. The Berry curvature resides mainly at the Γ point associated with the Zeeman gap opening (Fig. 3b), similar to the band inversion in the quantum anomalous Hall systems. Here we should emphasize that N_c does not physically correspond to a quantized Hall conductance because charge is not conserved in the BdG Hamiltonian[24]. Two chiral Majorana edge modes localized at two different edges clearly exist in the continuous superconducting gap due to the bulk-boundary correspondence (Fig. 3c and 3d). The propagation of chiral Majorana fermions could lead to same unitary transformation as that in braiding Majorana zero modes[70], and the deterministic creation and braiding of chiral edge vortices in hybrid structures were elaborated[71].

We finally construct a phase diagram of the 0.1-hole-doped $Ge_{1-x}Mn_xTe$ monolayer in Fig. 4, to help guide future experimental detection of the predicted TSC phase formed by the superconducting Rashba bands. At the zero-temperature limit, the SC phase of the Rashba bands will be preserved for $x < x_c = 0.017\%$ and the TSC phase will arise when $x > x_{min} = 0.014\%$, where the pre-condition of $\delta_z/2 > \Delta$ can be met (Supplementary Fig. 6d). At finite temperature, both the ferromagnetic and SC order should exist simultaneously for the formation of TSC phase. Referring to the ferromagnetic Curie temperatures T_c^{FM} of $Ge_{1-x}Mn_xTe$ that increases linearly with increasing Mn concentration up to $x = 0.2$ and can be fit by $T_c^{FM}(x) = 333 \times x$ K (Supplementary Fig. 7a)[39–44], we estimate $T_c^{FM}(x)$ and x-dependent T_c will cross over at $x'_{min} = 0.014\% = x_{min}$ (Supplementary Fig. 7b), too. Consequently, the TSC phase can be

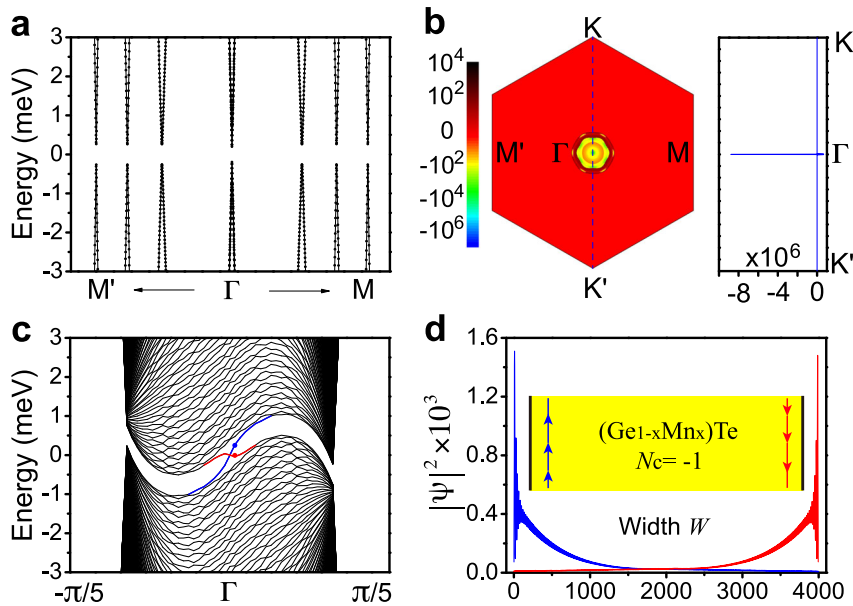**Fig. 3 The topological superconductivity of 0.1-hole-doped $Ge_{1-x}Mn_xTe$ monolayer. a** The dispersion relation of quasi-particles calculated by the first-principles BdG Hamiltonian. **b** The distribution of total Berry curvatures for the states below the superconducting gap in the first BZ (left panel) and along the line of K-Γ-K' (right panel). **c** The energy spectra of quasi-particles in a nanoribbon with the width (W) of 4000 primitive cells. The chiral Majorana edge modes are highlighted by red and blue lines. **d** The spatial distributed probability density of the in-gap states indicted by red and blue dot in (**c**). The inset is a schematic diagram of chiral Majorana edge modes with different propagation direction on opposite edges.
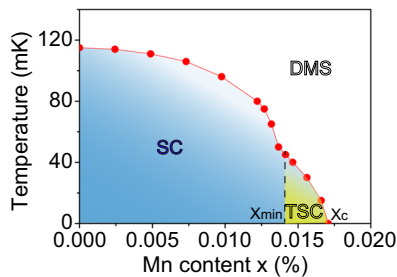

Fig. 4 The schematic phase diagram of the 0.1-hole-doped $Ge_{1-x}Mn_xTe$ monolayer. The yellow shaded region marks the TSC phase.

formed for $x_{min} < x < x_c$ at the temperature where the SC order occurs. Given that the non-trivial phase can be readily realized in non-centrosymmetric SCs when p-wave component is stronger than s-wave[22], our results indicate the TSC phase of $Ge_{1-x}Mn_xTe$ monolayer could be robust against parity mixing of Cooper pairs. We suggest preparing the desired $Ge_{1-x}Mn_xTe$ monolayer on BaF_2 (111) substrate[39–44] by molecular beam epitaxy since the growth is known to start in a 2D manner[41]. We anticipate that the chiral Majorana edge modes of $Ge_{1-x}Mn_xTe$ monolayer can be detected using Josephson effect[5] or charge transport[72], and controlled by magnetic flux[73]. The effects of magnetic anisotropy and GeTe film thickness on the TSC phase are discussed in Supplementary Note 4 and Note 5.

Lastly, in addition to the monolayer $Ge_{1-x}Mn_xTe$ we demonstrated here, we suggest two more candidate materials for Class D TSC. Firstly, since the heterostructures of $MnBi_2Te_4/Bi_2Te_3$[74,75] and $Bi_2Te_3/NbSe_2$[34,76] have already been fabricated, the $MnBi_2Te_4/Bi_2Te_3/NbSe_2$ hold high possibility to be synthesized. We demonstrate that this type of heterostructures with magnetized topological surface states are also a Class D TSC characterized with non-zero Chern number (Supplementary

Note 6)[77]. Secondly, it was experimentally reported the desired Rashba-Zeeman splitting can be alternatively achieved by the magnetic order in the Si-terminated surface of $HoRh_2Si_2$[78]. With a spin-singlet Cooper pairing being tunneled into this surface state by superconducting proximity effect, the Class D TSC will be readily emerging. By applying our developed first-principles BdG Hamiltonian approach, a complete phase diagram of these systems can be constructed in the near future.

METHODS

Details of the first-principles calculations

The Vienna ab initio simulation pack[79,80] was utilized to calculate the electronic property of normal states based on the density-functional theory. The exchange-correlation of electrons was treated within the generalized gradient approximation in the form of Perdew-Burke-Ernzerhof[81]. The atomic structures of GeTe monolayer and thin film was set up by introducing a vacuum region of more than 15 Å to avoid the interactions between neighboring images. Structural relaxations and self-consistent calculations as well as the Zeeman gap calculations were performed on a uniform $30 \times 30 \times 1$ ($18 \times 18 \times 18$) **k**-point sampling of the first BZ for monolayer (bulk) GeTe. The energy cutoff was set to 400 eV for plane-wave basis. The dipole correction was used to cancel the artificial electric field imposed by the periodic boundary condition of GeTe thin film.

The QUANTUM ESPRESSO package[82] was used to calculate the phonon spectra and EPC strength based on the density-functional perturbation theory[83] as well as fit the first-principles band structure by interfacing with the WANNIER90-2.1 code[58]. The Optimized Norm-Conserving Vanderbilt Pseudopotential[84] was employed and the kinetic energy cutoff was set to 100 Ry for wave functions. The hole doping was simulated by removing electrons from intrinsic GeTe monolayer and introducing the compensating jellium background to avoid divergence. The dynamic matrix and phonon frequency are computed on a $18 \times 18 \times 1$ **q**-point mesh with a $18 \times 18 \times 1$ **k**-point sampling, and a finer $36 \times 36 \times 1$ **k**-point grid is used in the EPC calculations, where the DOS is converged (Supplementary Fig. 2b). Other **q/k**-point samplings (Supplementary Table 1) are also employed to check the convergence of EPC calculations. The phonon DOS $F(\omega)$ and the isotropic Eliashberg spectral function $\alpha^2F(\omega)$ as well as the cumulative frequency-dependent EPC strength $\lambda(\omega)$ are calculated using a $60 \times 60 \times 1$ **q**-point sampling by means of the Fourier interpolation.

Specifically, the $\mathbf{q}$- and v-resolved EPC strength $\lambda_{\mathbf{q}v}$ is given by:

$$\lambda_{\mathbf{q}v} = \frac{1}{N_F \omega_{\mathbf{q}v}} \sum_{mn,\mathbf{k}} W_{\mathbf{k}} |g_{mn,v}(\mathbf{k},\mathbf{q})|^2 \delta(\varepsilon_{n\mathbf{k}})\delta(\varepsilon_{m\mathbf{k}+\mathbf{q}}) \quad (5)$$

$$g_{mn,v}(\mathbf{k},\mathbf{q}) = \left(\frac{\hbar}{2M_0\omega_{\mathbf{q}v}}\right)^{1/2} \langle \psi_{m\mathbf{k}+\mathbf{q}} |\partial_{\mathbf{q}v}\Xi| \psi_{n\mathbf{k}} \rangle \quad (6)$$

where N_F is the electronic DOS at the Fermi level, $W_{\mathbf{k}}$ is the weight of wavevector $\mathbf{k}$, $\varepsilon_{n\mathbf{k}}$ is the eigenvalue for electronic wavefunction $\psi_{n\mathbf{k}}$ with band index n and wavevector $\mathbf{k}$, $\omega_{\mathbf{q}v}$ is the frequency of a phonon branch v at wavevector $\mathbf{q}$, $\hbar$ is the reduced Planck constant, and M_0 is the ionic mass. $g_{mn,v}(\mathbf{k},\mathbf{q})$ represents the scattering amplitude between the electronic states with wavefunction $\psi_{n\mathbf{k}}$ and $\psi_{m\mathbf{k}+\mathbf{q}}$, induced by derivative $(\partial_{\mathbf{q}v}\Xi)$ of the self-consistent potential associated with phonon $\omega_{\mathbf{q}v}$. δ is the Dirac delta function. The frequency ω dependent isotropic Eliashberg spectral function $\alpha^2F(\omega)$ and the cumulative EPC strength $\lambda(\omega)$ are then calculated from:

$$\alpha^2F(\omega) = \frac{1}{2}\sum_{\mathbf{q}v} W_{\mathbf{q}}\omega_{\mathbf{q}v}\lambda_{\mathbf{q}v}\delta(\omega - \omega_{\mathbf{q}v}) \quad (7)$$

$$\lambda(\omega) = 2\int_0^\omega d\omega' \frac{\alpha^2F(\omega')}{\omega'} \quad (8)$$

Here $W_{\mathbf{q}}$ is the weight of wavevector $\mathbf{q}$. The total EPC constant λ equals to $\lambda(\omega_{max})$ with ω_{max} being the maximum of phonon frequency.

Constructing the BdG Hamiltonian

To perform first-principles prediction of TSC, the main challenge is to construct a BdG Hamiltonian of superconducting quasi-particles from the electronic Hamiltonian of normal state. Here we propose a strategy to overcome this obstacle by employing the WFs $\varphi_{WFs} = (\varphi_{1\uparrow}, \varphi_{2\uparrow}, \cdots, \varphi_{i\uparrow}, \cdots, \varphi_{\aleph\uparrow}, \varphi_{1\downarrow}, \varphi_{2\downarrow}, \cdots, \varphi_{i\downarrow}, \cdots, \varphi_{\aleph\downarrow})^T$ of specific materials. Here i is the orbital index, and the total number of WFs is $2\aleph$. The starting point is the real-space Hamiltonian $H_{WFs}^{(\mathbf{R})}$ and its matrix element $h_{ij}^{(\mathbf{R})}$ represents the hopping between the ith and the jth WF connected by a vector of $\mathbf{R}$, which can be obtained by fitting the first-principles band structures of specific materials using WANNIER90-2.1 code without performing minimization procedure[58]. The matrix element $h_{ij}(\mathbf{k})$ of momentum-space Hamiltonian $H_{WFs}(\mathbf{k})$ of normal state is then obtained through $h_{ij}(\mathbf{k}) = \sum_{\mathbf{R}} h_{ij}^{(\mathbf{R})} \times e^{i\mathbf{k}\cdot\mathbf{R}}$. Within the mean-field approximation, we can write the material-specific BdG Hamiltonian $H_{BdG}(\mathbf{k})$ (see Eq. 1) under the basis vector of $\varphi_{BdG} = (\varphi_{WFs}, \varphi_{WFs}^\dagger)^T$. The matrix element of $-H_{WFs}^*(-\mathbf{k})$ in $H_{BdG}(\mathbf{k})$ has the form of $h_{IJ}(\mathbf{k}) = -h_{ij}^*(-\mathbf{k}) = -\sum_{\mathbf{R}} h_{ij}^{*(\mathbf{R})} \times e^{i\mathbf{k}\cdot\mathbf{R}}$ with $I = i + 2\aleph$ and $J = j + 2\aleph$. The constructed $H_{BdG}(\mathbf{k})$ is a $4\aleph \times 4\aleph$ matrix with the particle-hole symmetry $PH_{BdG}(\mathbf{k})P^{-1} = -H_{BdG}^*(-\mathbf{k})$, where $P = \tau^x \otimes I_{2\aleph \times 2\aleph}$ and τ^x is the Pauli matrix in particle-hole space.

For the materials with external/internal magnetism, we first add a Zeeman term $\mathbf{B}$ in $H_{WFs}(\mathbf{k})$ using the vector of Pauli matrix $\boldsymbol{\sigma}$ in spin space: $H_{WFs}^{\mathbf{B}}(\mathbf{k}) = \mathbf{B}\boldsymbol{\sigma} \otimes I_{\aleph \times \aleph} + H_{WFs}(\mathbf{k})$. Then the first-principles BdG Hamiltonian $H_{BdG}^{\mathbf{B}}(\mathbf{k})$ without TRS can be constructed for a specific material by using the above procedure. We should emphasize that the above construction procedure is practically also applicable to materials with revelatively strong SOC. It is noted that the WFs, rather than the maximally localized WFs, are obtained by the WANNIER90 code without minimization procedure, so that the resulting WFs can be approximately seperated into up (majority) and down (minority) pseudospin orbitals in the presence of SOC. This treatment has been widely adopted in the WF-based methods for investigation of topological materials, such as WannierTools[85]. Here we develop another route to quantifying realistic conditions of TSC by solving self-consistently BdG equation based on WFs.

Formulating the gap equation

Under the basis of $\Psi_{\mathbf{k}} = (c_{1,\mathbf{k}}, c_{2,\mathbf{k}}, \cdots, c_{i,\mathbf{k}}, \cdots, c_{1,-\mathbf{k}}^\dagger, c_{2,-\mathbf{k}}^\dagger, \cdots, c_{i,-\mathbf{k}}^\dagger, \cdots)^T$, the multi-band Hamiltonian with s-wave pairing can be written as:

$$H = \sum_{\mathbf{k}>0} \Psi_{\mathbf{k}}^\dagger H_{BdG}(\mathbf{k})\Psi_{\mathbf{k}} \quad (9)$$

$$H_{BdG}(\mathbf{k}) = \begin{pmatrix} h(\mathbf{k}) & -\Delta \\ \Delta & -h^*(-\mathbf{k}) \end{pmatrix} \quad (10)$$

With the relation of $\frac{\partial H}{\partial \Delta_{ij}} = -\sum_{\mathbf{k}} \left(c_{i,\mathbf{k}}^\dagger c_{j,-\mathbf{k}}^\dagger + c_{j,-\mathbf{k}}c_{i,\mathbf{k}}\right)$, we can derive the gap equation of Δ_{ij} as:

$$\Delta_{ij} = \frac{g_{ij}}{V}\sum_{\mathbf{k}} \langle c_{j,-\mathbf{k}}c_{i,\mathbf{k}}\rangle = -\frac{g_{ij}}{2V} Tr\left[e^{-\beta H}\frac{\partial H}{\partial \Delta_{ij}}\right]/Tr\left[e^{-\beta H}\right] = \frac{g_{ij}}{2\beta V}\frac{\partial}{\partial \Delta_{ij}}\ln Tr\left[e^{-\beta H}\right] \quad (11)$$

Here $\beta = \frac{1}{k_BT}$. Diagonalizing the Hamiltonian H into the form of $H = \sum_{\mathbf{k},l} E_{l,\mathbf{k}}d_{l,\mathbf{k}}^\dagger d_{l,\mathbf{k}}$, we have

$$\Delta_{ij} = \frac{g_{ij}}{2\beta V}\frac{\partial}{\partial \Delta_{ij}}\ln \sum_{\{\varsigma_{l,\mathbf{k}}=0,1\}} \left[e^{-\beta\sum_{l,\mathbf{k}>0} E_{l,\mathbf{k}}\varsigma_{l,\mathbf{k}}}\right] = \frac{g_{ij}}{2\beta V}\frac{\partial}{\partial \Delta_{ij}}\sum_{l,\mathbf{k}>0}\ln\left(1 + e^{-\beta E_{l,\mathbf{k}}}\right)$$

$$= -\frac{g_{ij}}{2V}\sum_{l,\mathbf{k}>0}\frac{1}{1+e^{\beta E_{l,\mathbf{k}}}}\frac{\partial E_{l,\mathbf{k}}}{\partial \Delta_{ij}} \quad (12)$$

Solving this gap equation self-consistently enables us to estimates the superconducting transition temperature T_c and the critical magnetic field/doping-concentration of specific materials based on the material-specific BdG Hamiltonian $H_{BdG}(\mathbf{k})$ with/without TRS constructed from the state-of-art first-principles approach.

To confirm the above derivation, we apply the derived gap equation to the single-band Hamiltonian with s-wave pairing:

$$H_{BdG}(\mathbf{k}) = \begin{pmatrix} \varepsilon_{\mathbf{k}} & 0 & 0 & \Delta \\ 0 & \varepsilon_{\mathbf{k}} & -\Delta & 0 \\ 0 & -\Delta & -\varepsilon_{-\mathbf{k}} & 0 \\ \Delta & 0 & 0 & -\varepsilon_{-\mathbf{k}} \end{pmatrix} \quad (13)$$

Its eigenvalues are $E_{1,\mathbf{k}} = E_{2,\mathbf{k}} = \sqrt{\Delta^2 + \varepsilon_{\mathbf{k}}^2}$ and $E_{3,\mathbf{k}} = E_{4,\mathbf{k}} = -\sqrt{\Delta^2 + \varepsilon_{\mathbf{k}}^2}$ when the eigenvalues of normal electronic state satisfy $\varepsilon_{\mathbf{k}} = \varepsilon_{-\mathbf{k}}$. Substituting the four eigenvalues into the derived gap equation, we obtain the well-known gap equation of single-band s-wave superconductor:[60]

$$1 = \frac{g}{V}\sum_{\mathbf{k}>0}\frac{1}{\sqrt{\Delta^2 + \varepsilon_{\mathbf{k}}^2}}\tanh\left(\frac{\beta}{2}\sqrt{\Delta^2 + \varepsilon_{\mathbf{k}}^2}\right) \quad (14)$$

DATA AVAILABILITY

All data needed to evaluate the conclusions of this paper are available within the paper and Supplementary Information.

CODE AVAILABILITY

The central code used in this paper is the WANNIER90 code. Detailed information related to the license and user guide are available at http://www.wannier.org.

REFERENCES

1. Majorana, E. Teoria simmetrica dell'elettrone e del positrone. *Il Nuovo Cim. (1924-1942)* **14**, 171 (2008).
2. Ivanov, D. A. Non-Abelian Statistics of Half-Quantum Vortices in p-Wave Superconductors. *Phys. Rev. Lett.* **86**, 268–271 (2001).
3. Nayak, C., Simon, S. H., Stern, A., Freedman, M. & Das Sarma, S. Non-Abelian anyons and topological quantum computation. *Rev. Mod. Phys.* **80**, 1083–1159 (2008).
4. Volovik, G. E. Fermion zero modes on vortices in chiral superconductors. *J. Exp. Theor. Phys. Lett.* **70**, 609–614 (1999).
5. Jiang, L. et al. Unconventional Josephson Signatures of Majorana Bound States. *Phys. Rev. Lett.* **107**, 236401 (2011).
6. Tewari, S., Zhang, C., Das Sarma, S., Nayak, C. & Lee, D.-H. Testable Signatures of Quantum Nonlocality in a Two-Dimensional Chiral p-Wave Superconductor. *Phys. Rev. Lett.* **100**, 027001 (2008).
7. Wang, Z., Qi, X.-L. & Zhang, S.-C. Topological field theory and thermal responses of interacting topological superconductors. *Phys. Rev. B* **84**, 014527 (2011).
8. Lei, C., Chen, H. & MacDonald, A. H. Ultrathin Films of Superconducting Metals as a Platform for Topological Superconductivity. *Phys. Rev. Lett.* **121**, 227701 (2018).
9. Wang, Z. et al. Topological nature of the FeSe$_{0.5}$Te$_{0.5}$ superconductor. *Phys. Rev. B* **92**, 115119 (2015).

10. Wang, Z. F. et al. Topological edge states in a high-temperature superconductor FeSe/SrTiO$_3$(001) film. *Nat. Mater.* **15**, 968 (2016).

11. Zhang, J.-F., Guo, P.-J., Gao, M., Liu, K. & Lu, Z.-Y. β-RhPb$_2$: a topological superconductor candidate. *Phys. Rev. B* **99**, 045110 (2019).

12. Guo, P.-J. et al. LnPd$_2$Sn (Ln = Sc, Y, Lu) class of Heusler alloys for topological superconductivity. Preprint at https://arxiv.org/abs/1811.06401 (2018).

13. Jin, K.-H. et al. Topological superconducting phase in high-T$_c$ superconductor MgB$_2$ with Dirac-nodal-line fermions. *npj Comput Mater* **5**, 57 (2019).

14. Sau, J. D., Halperin, B. I., Flensberg, K. & Das Sarma, S. Number conserving theory for topologically protected degeneracy in one-dimensional fermions. *Phys. Rev. B* **84**, 144509 (2011).

15. Lapa, M. F. & Levin, M. Rigorous Results on Topological Superconductivity with Particle Number Conservation. *Phys. Rev. Lett.* **124**, 257002 (2020).

16. Zhang, X., Zhou, Y., Cui, B., Zhao, M. & Liu, F. Theoretical Discovery of a Superconducting Two-Dimensional Metal-Organic Framework. *Nano Lett.* **17**, 6166–6170 (2017).

17. Zhang, X., Zhao, M. & Liu, F. Enhancing superconductivity in bulk β-Bi$_2$Pd by negative pressure induced by quantum electronic stress. *Phys. Rev. B* **100**, 104527 (2019).

18. Read, N. & Green, D. Paired states of fermions in two dimensions with breaking of parity and time-reversal symmetries and the fractional quantum Hall effect. *Phys. Rev. B* **61**, 10267–10297 (2000).

19. Kitaev, A. Y. Unpaired Majorana fermions in quantum wires. *Phys. -Usp.* **44**, 131–136 (2001).

20. Mackenzie, A. P. & Maeno, Y. The superconductivity of Sr$_2$RuO$_4$ and the physics of spin-triplet pairing. *Rev. Mod. Phys.* **75**, 657–712 (2003).

21. Sasaki, S. & Mizushima, T. Superconducting doped topological materials. *Phys. C.* **514**, 206–217 (2015).

22. Sato, M. & Fujimoto, S. Topological phases of noncentrosymmetric superconductors: edge states, Majorana fermions, and non-Abelian statistics. *Phys. Rev. B* **79**, 094504 (2009).

23. Fu, L. & Kane, C. L. Superconducting Proximity Effect and Majorana Fermions at the Surface of a Topological Insulator. *Phys. Rev. Lett.* **100**, 096407 (2008).

24. Qi, X.-L., Hughes, T. L. & Zhang, S.-C. Chiral topological superconductor from the quantum Hall state. *Phys. Rev. B* **82**, 184516 (2010).

25. Lutchyn, R. M., Sau, J. D. & Das Sarma, S. Majorana Fermions and a Topological Phase Transition in Semiconductor-Superconductor Heterostructures. *Phys. Rev. Lett.* **105**, 077001 (2010).

26. Oreg, Y., Refael, G. & von Oppen, F. Helical Liquids and Majorana Bound States in Quantum Wires. *Phys. Rev. Lett.* **105**, 177002 (2010).

27. Sato, M., Takahashi, Y. & Fujimoto, S. Non-Abelian Topological Order in s-Wave Superfluids of Ultracold Fermionic Atoms. *Phys. Rev. Lett.* **103**, 020401 (2009).

28. Sau, J. D., Tewari, S., Lutchyn, R. M., Stanescu, T. D. & Das Sarma, S. Non-Abelian quantum order in spin-orbit-coupled semiconductors: Search for topological Majorana particles in solid-state systems. *Phys. Rev. B* **82**, 214509 (2010).

29. Sau, J. D., Lutchyn, R. M. & Tewari, S. & Das Sarma, S. Generic New Platform for Topological Quantum Computation Using Semiconductor Heterostructures. *Phys. Rev. Lett.* **104**, 040502 (2010).

30. Lutchyn, R. M. et al. Majorana zero modes in superconductor-semiconductor heterostructures. *Nat. Rev. Mater.* **3**, 52–68 (2018).

31. Nadj-Perge, S. et al. Observation of Majorana fermions in ferromagnetic atomic chains on a superconductor. *Science* **346**, 602 (2014).

32. Ménard, G. C. et al. Two-dimensional topological superconductivity in Pb/Co/Si (111). *Nat. Commun.* **8**, 2040 (2017).

33. Kezilebieke, S. et al. Topological superconductivity in a designer ferromagnet-superconductor van der Waals heterostructure. *Nature* **588**, 424–428 (2020).

34. Xu, J.-P. et al. Experimental Detection of a Majorana Mode in the core of a Magnetic Vortex inside a Topological Insulator-Superconductor Bi$_2$Te$_3$/NbSe$_2$ Heterostructure. *Phys. Rev. Lett.* **114**, 017001 (2015).

35. Jäck, B. et al. Observation of a Majorana zero mode in a topologically protected edge channel. *Science* **364**, 1255 (2019).

36. Zhu, S. et al. Nearly quantized conductance plateau of vortex zero mode in an iron-based superconductor. *Science* **367**, 189 (2020).

37. Narayan, V., Nguyen, T.-A., Mansell, R., Ritchie, D. & Mussler, G. Interplay of spin-orbit coupling and superconducting correlations in germanium telluride thin films. *Phys. Status Solidi RRL* **10**, 253–259 (2016).

38. Lv, Y.-F. et al. Experimental signature of topological superconductivity and Majorana zero modes on β-Bi$_2$Pd thin films. *Sci. Bull.* **62**, 852–856 (2017).

39. Fukuma, Y., Asada, H., Nishimura, N. & Koyanagi, T. Ferromagnetic properties of IV–VI diluted magnetic semiconductor Ge$_{1-x}$Mn$_x$Te films prepared by radio frequency sputtering. *J. Appl. Phys.* **93**, 4034–4039 (2003).

40. Chen, W. Q., Teo, K. L., Jalil, M. B. A. & Liew, T. Compositional dependencies of ferromagnetic Ge$_{1-x}$Mn$_x$Te grown by solid-source molecular-beam epitaxy. *J. Appl. Phys.* **99**, 08D515 (2006).

41. Hassan, M. et al. Molecular beam epitaxy of single phase GeMnTe with high ferromagnetic transition temperature. *J. Cryst. Growth* **323**, 363–367 (2011).

42. Cochrane, R. W., Plischke, M. & Ström-Olsen, J. O. Magnetization studies of (GeTe)$_{1-x}$(MnTe)x pseudobinary alloys. *Phys. Rev. B* **9**, 3013–3021 (1974).

43. Chen, W. Q. et al. Optical, magnetic, and transport behaviors of Ge$_{1-x}$Mn$_x$Te ferromagnetic semiconductors grown by molecular-beam epitaxy. *J. Appl. Phys.* **104**, 063912 (2008).

44. Fukuma, Y. et al. Carrier-induced ferromagnetism in Ge$_{0.92}$Mn$_{0.08}$Te epilayers with a Curie temperature up to 190 K. *Appl. Phys. Lett.* **93**, 252502 (2008).

45. Hein, R. A., Gibson, J. W., Mazelsky, R., Miller, R. C. & Hulm, J. K. Superconductivity in Germanium Telluride. *Phys. Rev. Lett.* **12**, 320–322 (1964).

46. Smith, J. L. & Stiles, P. J. Superconducting energy gap in semiconducting GeTe. *J. Low. Temp. Phys.* **26**, 101–110 (1977).

47. Chattopadhyay, T., Boucherle, J. X. & vonSchnering, H. G. Neutron diffraction study on the structural phase transition in GeTe. *J. Phys. C.* **20**, 1431–1440 (1987).

48. Krempaský, J. et al. Entanglement and manipulation of the magnetic and spin-orbit order in multiferroic Rashba semiconductors. *Nat. Commun.* **7**, 13071 (2016).

49. Zhang, P. et al. Sonication-assisted liquid-phase exfoliated α-GeTe: a two-dimensional material with high Fe^{3+}. sensitivity. *Nanoscale* **10**, 15989–15997 (2018).

50. Qiao, M., Chen, Y., Wang, Y. & Li, Y. The germanium telluride monolayer: a two dimensional semiconductor with high carrier mobility for photocatalytic water splitting. *J. Mater. Chem. A* **6**, 4119–4125 (2018).

51. Wang, C. et al. Type-II Ising Superconductivity in Two-Dimensional Materials with Spin-Orbit Coupling. *Phys. Rev. Lett.* **123**, 126402 (2019).

52. LaShell, S., McDougall, B. A. & Jensen, E. Spin Splitting of an Au(111) Surface State Band Observed with Angle Resolved Photoelectron Spectroscopy. *Phys. Rev. Lett.* **77**, 3419–3422 (1996).

53. Koroteev, Y. M. et al. Strong Spin-Orbit Splitting on Bi Surfaces. *Phys. Rev. Lett.* **93**, 046403 (2004).

54. Krempasky, J. et al. Disentangling bulk and surface Rashba effects in ferroelectric α-GeTe. *Phys. Rev. B* **94**, 205111 (2016).

55. Przybylinska, H. et al. Magnetic-Field-Induced Ferroelectric Polarization Reversal in the Multiferroic Ge$_{1-x}$Mn$_x$Te Semiconductor. *Phys. Rev. Lett.* **112**, 047202 (2014).

56. Nordheim, L. Zur Elektronentheorie der Metalle. *I. Ann. Phys.* **401**, 607–640 (1931).

57. Si, C., Liu, Z., Duan, W. & Liu, F. First-Principles Calculations on the Effect of Doping and Biaxial Tensile Strain on Electron-Phonon Coupling in Graphene. *Phys. Rev. Lett.* **111**, 196802 (2013).

58. Mostofi, A. A. et al. An updated version of wannier90: a tool for obtaining maximally-localised Wannier functions. *Comput. Phys. Commun.* **185**, 2309–2310 (2014).

59. Morel, P. & Anderson, P. W. Calculation of the Superconducting State Parameters with Retarded Electron-Phonon Interaction. *Phys. Rev.* **125**, 1263–1271 (1962).

60. Bardeen, J., Cooper, L. N. & Schrieffer, J. R. Theory of Superconductivity. *Phys. Rev.* **108**, 1175–1204 (1957).

61. Floris, A., Sanna, A., Massidda, S. & Gross, E. K. U. Two-band superconductivity in Pb from ab initio calculations. *Phys. Rev. B* **75**, 054508 (2007).

62. Costanzo, D., Zhang, H., Reddy, B. A., Berger, H. & Morpurgo, A. F. Tunnelling spectroscopy of gate-induced superconductivity in MoS$_2$. *Nat. Nanotechnol* **13**, 483–488 (2018).

63. Ye, J. T. et al. Superconducting Dome in a Gate-Tuned Band Insulator. *Science* **338**, 1193 (2012).

64. Shelimova, L. E. & Plachkova, S. K. Estimation of the Debye Temperature of IV–VI Semiconductor Compounds and Rhombohedral (GeTe)$_{1-x}$((Ag$_2$Te)$_{1-y}$(Sb$_2$Te$_3$)y)x Solid Solutions (y = 0.6). *Phys. Status Solidi A* **104**, 679–685 (1987).

65. Peng, B. et al. Thermal conductivity of monolayer MoS$_2$, MoSe$_2$, and WS$_2$: interplay of mass effect, interatomic bonding and anharmonicity. *RSC Adv* **6**, 5767–5773 (2016).

66. Das, T. & Dolui, K. Superconducting dome in MoS$_2$ and TiSe$_2$ generated by quasiparticle-phonon coupling. *Phys. Rev. B* **91**, 094510 (2015).

67. Campi, D., Donadio, D., Sosso, G. C., Behler, J. & Bernasconi, M. Electron-phonon interaction and thermal boundary resistance at the crystal-amorphous interface of the phase change compound GeTe. *J. Appl. Phys.* **117**, 015304 (2015).

68. Lu, J. M. et al. Evidence for two-dimensional Ising superconductivity in gated MoS$_2$. *Science* **350**, 1353 (2015).

69. Rogacki, K. et al. Strong magnetic pair breaking in Mn-substituted MgB$_2$ single crystals. *Phys. Rev. B* **73**, 174520 (2006).

70. Lian, B., Sun, X.-Q., Vaezi, A., Qi, X.-L. & Zhang, S.-C. Topological quantum computation based on chiral Majorana fermions. *P. Natl Acad. Sci. USA* **115**, 10938 (2018).

71. Beenakker, C. W. J. et al. Deterministic Creation and Braiding of Chiral Edge Vortices. *Phys. Rev. Lett.* **122**, 146803 (2019).

72. He, Q. L. et al. Chiral Majorana fermion modes in a quantum anomalous Hall insulator–superconductor structure. *Science* **357**, 294 (2017).

73. Zhou, Y.-F., Hou, Z., Lv, P., Xie, X. & Sun, Q.-F. Magnetic flux control of chiral Majorana edge modes in topological superconductor. *Sci. China Phys. Mech.* **61**, 127811 (2018).

74. Rienks, E. D. L. et al. Large magnetic gap at the Dirac point in Bi_2Te_3/$MnBi_2Te_4$ heterostructures. *Nature* **576**, 423–428 (2019).

75. Deng, H. et al. High-temperature quantum anomalous Hall regime in a $MnBi_2Te_4$/Bi_2Te_3 superlattice. *Nat. Phys* **17**, 36–42 (2021).

76. Xu, J.-P. et al. Artificial Topological Superconductor by the Proximity Effect. *Phys. Rev. Lett.* **112**, 217001 (2014).

77. Zhang, X. & Liu, F. Prediction of Majorana edge states from magnetized topological surface states. *Phys. Rev. B* **103**, 024405 (2021).

78. Generalov, A. et al. Spin Orientation of Two-Dimensional Electrons Driven by Temperature-Tunable Competition of Spin-Orbit and Exchange-Magnetic Interactions. *Nano Lett.* **17**, 811–820 (2017).

79. Kresse, G. & Furthmüller, J. Efficient iterative schemes for ab initio total-energy calculations using a plane-wave basis set. *Phys. Rev. B* **54**, 11169–11186 (1996).

80. Kresse, G. & Hafner, J. Ab initiomolecular dynamics for open-shell transition metals. *Phys. Rev. B* **48**, 13115–13118 (1993).

81. Perdew, J. P., Burke, K. & Ernzerhof, M. Generalized Gradient Approximation Made Simple. *Phys. Rev. Lett.* **77**, 3865–3868 (1996).

82. Paolo, G. et al. QUANTUM ESPRESSO: a modular and open-source software project for quantum simulations of materials. *J. Phys.: Conden. Matter* **21**, 395502 (2009).

83. Baroni, S., de Gironcoli, S., Dal Corso, A. & Giannozzi, P. Phonons and related crystal properties from density-functional perturbation theory. *Rev. Mod. Phys.* **73**, 515–562 (2001).

84. Hamann, D. R. Optimized norm-conserving Vanderbilt pseudopotentials. *Phys. Rev. B* **88**, 085117 (2013).

85. Wu, Q., Zhang, S., Song, H.-F., Troyer, M. & Soluyanov, A. A. WannierTools: an open-source software package for novel topological materials. *Comput. Phys. Commun.* **224**, 405–416 (2018).

AUTHOR CONTRIBUTIONS

F.L. and Z.L. conceived and directed the project. X.Z. performed the first-principles calculations, constructed the first-principles BdG Hamiltonian, and calculated the data. J.M. formulated the superconducting gap Eq. 3. All authors analyzed and discussed the results. X.Z. and F.L. wrote the paper.

COMPETING INTERESTS

The authors declare no competing interests.

ADDITIONAL INFORMATION

Supplementary information The online version contains supplementary material available at https://doi.org/10.1038/s41524-021-00511-x.

Correspondence and requests for materials should be addressed to Z.L. or F.L.

Reprints and permission information is available at http://www.nature.com/reprints

Publisher's note Springer Nature remains neutral with regard to jurisdictional claims in published maps and institutional affiliations.